Optimized Hybrid Radial Kernels for Stable and Accurate Solutions of Volterra Integral Equations: A Meshless Approach

Tahereh Akbari[a], Mohsen Esmaeilbeigi[a,*], Davoud Moazami[a]

[a]*Faculty of Mathematical Sciences and Statistics, Malayer University, Malayer, Iran*

Abstract

A central challenge in kernel-based approximation theory is balancing accuracy with numerical stability. Hybrid kernels provide an effective solution to this trade-off. In this paper, we present a meshless scheme utilizing hybrid radial kernels (HRKs) to solve Volterra integral equations (VIEs). The solution is approximated using a discrete collocation method, where the HRK is formed by combining suitable base kernels with optimized weight parameters. These parameters are determined via the particle swarm optimization (PSO) algorithm, which minimizes the root-mean-square (RMS) error. We also provide a convergence analysis to confirm the method's theoretical reliability. Numerical experiments validate the approach, demonstrating its accuracy and stability compared to existing methods. The results show that this hybrid technique effectively reduces ill-conditioning in operational matrices while preserving high precision and stability across a range of shape parameter values.

Keywords: Volterra integral equations; Hybrid kernels; Particle swarm optimization; Accuracy; Stability.

1. Introduction

VIEs are a class of integral equations distinguished by their variable upper limits of integration, setting them apart from Fredholm-type equations [1]. VIEs have many applications in various areas such as:

- The following nonlinear Volterra integral equation (VIE) arises in the analysis of the neural networks with a post-inhibitory rebound [2],

$$u(x) = 1 + \int_0^x (x-t)^3 (4-x+t) e^{t-x} \frac{u^4(t)}{1 + 2u^2(t) + 2u^4(t)} dt, \quad x \in [0, 10].$$

- The following VIE arises in the analysis of the reflexion of sound pulses [3],

$$u(x) = f(x) - \int_0^x \frac{2}{(x-t+2)^2} g(u(t)) dt, \quad x \in [0, 40].$$

- Some nonlinear VIEs arise as a reformulation of initial value problems which occur in many problems of mathematical physics. For example, consider the Lane-Emden type equations arise in the analysis of the gravitational potential of the degenerate white-dwarf stars, the isothermal gas sphere, the

---

*Corresponding author

Email addresses: `MrsTahere_Akbari@yahoo.com` (Tahereh Akbari), `m.esmaeilbeigi@malayeru.ac.ir` (Mohsen Esmaeilbeigi), `davoud.moazami@stu.malayeru.ac.ir` (Davoud Moazami)

static stellar models in Newtonian gravity and other problems in the mathematical physics [3], which are defined as follows:

$$u'' + \frac{2}{s}u' + g(s)f(u) = h(s), \quad 0 < s < \infty,$$

subject to

$$u(0) = a, \quad u'(0) = 0,$$

where a is a constant and f, g and h are determined functions. The given Lane-Emden problem can be transformed into the following VIE [3, 4]

$$u(x) = a + \int_0^x \left(\frac{t^2}{x} - t\right)(g(u)f(u(t) - h(t)))dt, \quad x \in (0, \infty).$$

In this article, we focus on nonlinear VIEs in d-dimensional space, expressed as:

$$u(\mathbf{x}) - \lambda \int_{a_1}^{x_1} \cdots \int_{a_d}^{x_d} K(\mathbf{x}, \mathbf{y}, u(\mathbf{y})) \, d\mathbf{y} = f(\mathbf{x}), \tag{1}$$

where $\mathbf{x} \in \Omega \subset \mathbb{R}^d$, K is a continuously differentiable kernel, f is a continuous function, and $\lambda \neq 0$. Our objective is to determine the unknown function $u(\mathbf{x})$.

Numerical methods for solving VIEs have advanced significantly over time. Traditional approaches include collocation methods [2, 5], Galerkin techniques [6, 7], and spectral methods such as those using Chebyshev polynomials [8] or Jacobi polynomials [9]. More recent developments encompass wavelet-based schemes [10, 11, 12, 13], reproducing kernel Hilbert space methods [14], and specialized algorithms for singular [15] or multi-dimensional VIEs [16]. These methods provide a robust foundation for tackling the computational challenges posed by VIEs.

Among modern tools, meshless methods based on radial basis functions (RBFs) and radial kernels stand out as cutting-edge solutions. RBFs, first introduced with Hardy's multiquadrics [17] and later expanded to include forms like thin plate splines [18], excel in scattered data interpolation and are particularly effective for VIEs due to their dimension-independent formulation [17]. Meshless methods that leverage RBF offer significant advantages, especially for problems involving complex geometries or moving boundaries [19]. Their applications span partial differential equation (PDE) solutions in fluid dynamics [20], and thermal analysis [21], often outperforming traditional methods in accuracy and computational efficiency [22]. Also, the RBFs have been applied for the numerical solution of VIEs [23]. Furthermore, a meshless local Galerkin method was introduced in [24] as an effective means to solve VIEs derived from nonlinear fractional differential equations.

However, a key challenge in RBF-based methods is the trade-off between accuracy and numerical stability. As the shape parameter in RBFs decreases, interpolation accuracy increases, but the system matrix's condition number worsens, leading to numerical instability. To mitigate this, a range of modern strategies has been developed, including curvature-adaptive schemes [25], data-driven approaches leveraging neural networks or regression models [26], and Bayesian optimization techniques [27], which systematically tune the shape parameter to balance precision and stability. Additionally, the Hilbert–Schmidt SVD (HS-SVD) approach provides a stable mechanism for replacing a set of near-flat kernels

with scattered centres to a well-conditioned basis for exactly the same space [28, 29, 30]. These methods aim to balance accuracy and numerical stability more systematically than traditional trial and-error approaches.

Another stable approach to addressing ill-conditioning is the use of hybrid kernels [31], which provide an effective and attractive solution owing to their conceptual simplicity and ease of implementation. By combining smooth and non-smooth RBFs such as Gaussian and cubic kernels hybrid kernel methods improve the system's conditioning while maintaining high approximation accuracy. These methods have proven successful in applications such as temperature field reconstruction [32], neurodynamic modeling [33], and viscous flow analysis [34]. In this article, we employ the hybrid kernel technique to address the accuracy-stability trade-off in the numerical solution of nonlinear VIEs, leveraging its straightforward implementation and robust performance.

Our work introduces a novel approach to solving nonlinear VIEs in d-dimensions using hybrid kernels, focusing on three main contributions: a parameter-optimized collocation scheme, a formal convergence analysis, and comprehensive numerical validation demonstrating stability and accuracy across a range of shape parameters. This method enhances the meshless advantages of RBFs while overcoming limitations of traditional techniques [35]. The article is structured as follows:

- **Section 2**: Theoretical preliminaries of hybrid kernels.

- **Section 3**: Meshless implementation for solving VIEs.

- **Section 4**: Analytical convergence results.

- **Section 5**: Novel parameter selection methodology.

- **Section 6**: Numerical verification across dimensional cases.

- **Section 7**: Conclusions and future directions.

This structure guides readers through the theoretical foundations, practical implementation, and empirical validation of our approach, highlighting the hybrid kernel technique as a significant advancement in VIE solvers.

2. Theoretical preliminaries of hybrid kernels

This section presents the essential definitions and mathematical foundations of HRKs used in this study.

2.1. Interpolation by HRKs

Hybrid radial kernels provide a flexible framework for approximating functions in any dimension. We begin by defining radial kernels.

Definition 1. *[36] A kernel $\Phi : \mathbb{R}^d \to \mathbb{R}$ is termed radial if there exists a univariate function $\phi : [0, \infty) \to \mathbb{R}$ such that*

$$\Phi(\mathbf{x}) = \phi(r),$$

where $r = \|\mathbf{x}\|_2$ and $\| \cdot \|_2$ is the Euclidean norm on $\mathbb{R}^d$.

3

Let $\mathcal{X} = \{\mathbf{x}_i\}_{i=1}^n$ be a set of distinct nodes in a region $\Omega \subset \mathbb{R}^d$. To approximate a function $u(\mathbf{x})$ at a point $\mathbf{x} \in \Omega$ using the radial kernel $\Phi(\mathbf{x})$, we consider the linear combination:

$$u(\mathbf{x}) \approx \mathcal{P}_n u(\mathbf{x}) = \sum_{j=1}^n \alpha_j \phi(\|\mathbf{x} - \mathbf{x}_j\|_2), \quad \mathbf{x} \in \Omega. \tag{2}$$

The coefficients $\boldsymbol{\alpha} = [\alpha_1, \alpha_2, \ldots, \alpha_n]^T$ are determined by the interpolation conditions:

$$\mathcal{P}_n u(\mathbf{x}_i) = u(\mathbf{x}_i), \quad i = 1, 2, \ldots, n, \tag{3}$$

which lead to the linear system:

$$\mathbf{A}\boldsymbol{\alpha} = \mathbf{u}, \tag{4}$$

where $\mathbf{A} = [\phi(\|\mathbf{x}_i - \mathbf{x}_j\|_2)]_{i,j=1}^n$ and $\mathbf{u} = [u(\mathbf{x}_1), u(\mathbf{x}_2), \ldots, u(\mathbf{x}_n)]^T$.

Radial kernels can be classified into two main categories: infinitely smooth and piecewise smooth kernels, as shown in Table 1. Infinitely smooth kernels, such as Gaussian (GA) and inverse multiquadrics (IMQ), yield positive definite coefficient matrices $\mathbf{A}$ in (4). Multiquadrics (MQ) produce matrices with one positive eigenvalue and the rest negative, ensuring invertibility [28, 38, 39, 40, 41, 42]. Piecewise smooth kernels, such as thin plate splines (TPS) and cubic (CU), are symmetric and conditionally strictly positive definite. Therefore, lower degree polynomials

$$\Lambda(\boldsymbol{x}) = \sum_{k=1}^m \zeta_k p_k(\boldsymbol{x}),$$

are often required to ensure invertibility. In the above equation, the polynomials $p_1, \cdots, p_m$ form a basis for the $m = \begin{pmatrix} d + r - 1 \\ r - 1 \end{pmatrix}$-dimensional linear space $\Pi_{r-1}^d(\Omega)$ of polynomials of total degree less than or equal to $m - 1$ in d variables on the set Ω [36]. However, in most cases, radial kernels without augmented polynomials $\Lambda(\boldsymbol{x})$ are usually used where satisfactory results have been obtained without encountering singular matrices [34]. For this reason, the augmented polynomial terms are often removed [35, 37].

Based on the aforementioned categorization, we define the hybrid radial kernel (HRK) family as:

$$\psi_j(\mathbf{x}) = \alpha \Phi_j^\varepsilon(\mathbf{x}) + \beta \varphi_j(\mathbf{x}), \quad j = 1, 2, \ldots, n, \tag{5}$$

where $\Phi^\varepsilon(\mathbf{x}) = \phi(\varepsilon\|\mathbf{x}\|_2)$ is an infinitely smooth radial kernel with shape parameter ε, and $\varphi(\mathbf{x}) = \varpi(\|\mathbf{x}\|_2)$ is a piecewise smooth radial kernel without a shape parameter. The coefficients α and β are positive real numbers controlling the contribution of each kernel. Since scaling a radial kernel by a constant does not affect the interpolation algorithm [43], we normalize the HRK family using the ratio $\rho = \dfrac{\beta}{\alpha}$, leading to:

$$\psi_j^{\varepsilon,\rho}(\mathbf{x}) = \Phi_j^\varepsilon(\mathbf{x}) + \rho \varphi_j(\mathbf{x}), \quad j = 1, 2, \ldots, n. \tag{6}$$

The HRK family incorporates two parameters: the shape parameter ε and the weight parameter ρ, which balance accuracy and stability in the hybrid kernel method.

To approximate the unknown function $u(\mathbf{x})$ using HRKs, we define:

$$u(\mathbf{x}) \approx \mathcal{Q}_n u(\mathbf{x}) = \sum_{j=1}^n c_j \psi_j^{\varepsilon,\rho}(\mathbf{x}), \quad \mathbf{x} \in \Omega \subset \mathbb{R}^d, \tag{7}$$

where

4

$$\psi_j^{\varepsilon,\rho}(\mathbf{x}) = \Phi_j^\varepsilon(\mathbf{x}) + \rho\varphi_j(\mathbf{x}) = \phi(\varepsilon\|\mathbf{x} - \mathbf{x}_j\|_2) + \rho\varpi(\|\mathbf{x} - \mathbf{x}_j\|_2), \quad j = 1, 2, \ldots, n. \tag{8}$$

The coefficients $\mathbf{c} = [c_1, c_2, \ldots, c_n]^T$ are obtained by solving the linear system $\mathbf{\Gamma c} = \mathbf{u}$, where the hybrid kernel matrix $\mathbf{\Gamma} \in \mathbb{R}^{n \times n}$ is given by:

$$\mathbf{\Gamma}_{i,j} = \psi_j^{\varepsilon,\rho}(\mathbf{x}_i), \quad i, j = 1, \ldots, n.$$

Table 1: Some well-known radial kernels

Name of radial kernel	Definition
Infinitely smooth:	
Multiquadrics (MQ)	$\sqrt{\varepsilon^2 r^2 + 1}$
Inverse multiquadrics (IMQ)	$\dfrac{1}{\sqrt{\varepsilon^2 r^2 + 1}}$
Gaussian (GA)	$e^{-(\varepsilon r)^2}$
Piecewise smooth:	
Thin plate spline (TPS)	$r^2 \log(r)$
Cubic (CU)	r^3

2.2. Error Analysis for HRKs

To establish error bounds for HRK interpolation, we introduce the concept of native Hilbert spaces associated with radial kernels.

Theorem 1. *[36, 38] Let $\Phi \in L_1(\mathbb{R}^d) \cap C(\mathbb{R}^d)$ be a strictly positive integer with a real value. The corresponding real native Hilbert space associated with Φ can be expressed as:*

$$\mathcal{N}_\Phi(\mathbb{R}^d) = \left\{ f \in L_2(\mathbb{R}^d) \cap C(\mathbb{R}^d) : \frac{\hat{f}}{\sqrt{\hat{\Phi}}} \in L_2(\mathbb{R}^d) \right\},$$

with the inner product:

$$\langle f, g \rangle_{\mathcal{N}_\Phi(\mathbb{R}^d)} = (2\pi)^{-\frac{d}{2}} \int_{\mathbb{R}^d} \frac{\hat{f}(\omega)\overline{\hat{g}(\omega)}}{\hat{\Phi}(\omega)} \, d\omega,$$

where $\hat{f}$ is the Fourier transform of f.

The notion of native spaces extends to conditionally positive definite radial kernels; for details, see [36, 38]. To quantify the quality of the approximation, we define two indicators of data regularity:

Definition 2. *For a set of nodes $\mathcal{X} = \{\mathbf{x}_i\}_{i=1}^n$ contained in Ω, the fill distance is defined by:*

$$h_{\mathcal{X},\Omega} := \sup_{\mathbf{x} \in \Omega} \min_{1 \leq j \leq n} \|\mathbf{x} - \mathbf{x}_j\|_2.$$

Definition 3. *The separation distance of $\mathcal{X} = \{\mathbf{x}_i\}_{i=1}^n$ is:*

$$q_{\mathcal{X}} := \frac{1}{2} \min_{i \neq j} \|\mathbf{x}_i - \mathbf{x}_j\|_2.$$

Remark 1. *A set $\mathcal{X}$ is quasi-uniform with respect to a constant $c_{qu} > 0$ if:*

$$q_{\mathcal{X}} \leq h_{\mathcal{X},\Omega} \leq c_{qu} q_{\mathcal{X}}.$$

The following theorem provides an error bound for interpolation using conditionally positive definite kernels:

Theorem 2. *[36, 38] Suppose $\Omega \subset \mathbb{R}^d$ is a bounded domain satisfying an interior cone condition. Let Φ be conditionally positive definite, and denote by $\mathcal{P}_n u$ the interpolant of $u \in \mathcal{N}_\Phi(\Omega)$ constructed on the quasi-uniform set $\mathcal{X} = \{\mathbf{x}_i\}_{i=1}^n$. If all derivatives of Φ up to order $2k$ are continuous on $\Omega \times \Omega$, then there exist constants $h_0 > 0$ and $C > 0$ such that:*

$$\|u - \mathcal{P}_n u\|_{L^\infty(\Omega)} \le C\sqrt{C_\Phi}\, h_{\mathcal{X},\Omega}^k \|u\|_{\mathcal{N}_\Phi(\Omega)},$$

provided that $h_{\mathcal{X},\Omega} \le h_0$, where:

$$C_\Phi = \max_{|\gamma|=2k}\; \max_{\mathbf{s},\mathbf{z}\in\Omega\cap B(\mathbf{x},c_2 h_{\mathcal{X},\Omega})} |D_2^\gamma \Phi(\mathbf{s},\mathbf{z})|.$$

Applying this to hybrid kernels, we have:

Corollary 1. *Since $\Phi^\varepsilon(\mathbf{x})$ and $\varphi(\mathbf{x})$ are strictly and conditionally positive definite kernels, their linear combination $\psi^{\varepsilon,\rho}(\mathbf{x}) = \Phi^\varepsilon(\mathbf{x}) + \rho\varphi(\mathbf{x})$ is conditionally positive definite for all $\rho > 0$ [38]. Thus, by Theorem 2, if $\psi^{\varepsilon,\rho} \in C^{2k}(\Omega \times \Omega)$, there exist positive constants $\tilde{h}_0$ and $\tilde{C}$ such that:*

$$\|u - \mathcal{Q}_n u\|_{L^\infty(\Omega)} \le \tilde{C}\sqrt{\tilde{C}_{\psi^{\varepsilon,\rho}}}\, h_{\mathcal{X},\Omega}^k \|u\|_{\mathcal{N}_{\psi^{\varepsilon,\rho}}(\Omega)},$$

where $u \in \mathcal{N}_{\psi^{\varepsilon,\rho}}(\Omega)$, $\mathcal{Q}_n u$ is the HRK interpolation of u on $\mathcal{X}$, $\mathcal{N}_{\psi^{\varepsilon,\rho}}(\Omega)$ is the native space of $\psi^{\varepsilon,\rho}$, $h_{\mathcal{X},\Omega} \le \tilde{h}_0$, and:

$$\tilde{C}_{\psi^{\varepsilon,\rho}} = \max_{|\gamma|=2k}\; \max_{\mathbf{s},\mathbf{z}\in\Omega\cap B(\mathbf{x},c_2 h_{\mathcal{X},\Omega})} |D_2^\gamma \psi^{\varepsilon,\rho}(\mathbf{s},\mathbf{z})|.$$

3. Meshless Implementation for Solving VIEs by HRKs

In this part, we develop a meshfree approach based on hybrid radial kernels to tackle nonlinear VIEs of the second kind. Extending prior radial kernel methods, this approach incorporates HRKs to enhance stability and accuracy, addressing limitations of traditional kernels.

Define the operator $\mathcal{F} : C(\Omega) \to C(\Omega)$ as:

$$\mathcal{F}u = \lambda \int_{a_1}^{x_1} \cdots \int_{a_d}^{x_d} K(\mathbf{x}, \mathbf{y}, u(\mathbf{y})) + f(\mathbf{x})\, d\mathbf{y}, \quad \mathbf{x}, \mathbf{y} \in \Omega, \tag{9}$$

where $\Omega = [a_1, b_1] \times \cdots \times [a_d, b_d] \subset \mathbb{R}^d$, and K satisfies the following Lipschitz condition [44]:

$$|K(\mathbf{x}, \mathbf{y}, u_1) - K(\mathbf{x}, \mathbf{y}, u_2)| \le L_1 |u_1 - u_2|,$$

for all $\mathbf{x}, \mathbf{y} \in \Omega$ and $u_1, u_2 \in \mathbb{R}$ with the Lipschitz constant L_1 being independent of u_1 and u_2. Using the operator (9), we can rewrite (1) as:

$$u = \mathcal{F}u. \tag{10}$$

Given n collocation points $\mathcal{X} = \{\mathbf{x}_i\}_{i=1}^n$ in Ω, the solution is approximated as:

$$u_n(\mathbf{x}) = \sum_{j=1}^n c_j \psi_j^{\varepsilon,\rho}(\mathbf{x}), \quad \mathbf{x} \in \Omega, \tag{11}$$

6

where $\psi_j^{\varepsilon,\rho}(\mathbf{x}) = \psi^{\varepsilon,\rho}(\|\mathbf{x} - \mathbf{x}_j\|_2)$ are HRKs (see Section 2). The coefficients $\{c_j\}$ satisfy:

$$\sum_{j=1}^{n} c_j \psi_j^{\varepsilon,\rho}(\mathbf{x}_i) - \lambda \int_{a_1}^{x_{i1}} \cdots \int_{a_d}^{x_{id}} K\left(\mathbf{x}_i, \mathbf{y}, \sum_{j=1}^{n} c_j \psi_j^{\varepsilon,\rho}(\mathbf{y})\right) d\mathbf{y} = f(\mathbf{x}_i), \quad i = 1, \dots, n. \tag{12}$$

Integrals are approximated numerically, with techniques varying by dimension.

3.1. One-Dimensional VIEs

For $\Omega = [a, b]$, the integral in (12) is approximated using a m-point composite Gauss-Legendre (CGL) quadrature with P subdivisions, yielding:

$$\sum_{j=1}^{n} \hat{c}_j \psi_j^{\varepsilon,\rho}(x_i) - \lambda \sum_{q=1}^{P} \sum_{k=1}^{m} w_k \frac{\Delta y(x_i)}{2} K\left(x_i, \theta_k^q(x_i), \sum_{j=1}^{n} \hat{c}_j \psi_j^{\varepsilon,\rho}(\theta_k^q(x_i))\right) = f(x_i), \tag{13}$$

where $\Delta y(x_i) = \frac{x_i - a}{P}$, $\theta_k^q(x_i) = \frac{\Delta y(x_i)}{2} v_k + (q - \frac{1}{2})\Delta y(x_i)$, and $\{v_k, w_k\}$ are Gauss-Legendre nodes and weights on $[-1, 1]$. The HRKs' differentiability ensures quadrature accuracy. After solving (13), the approximate solution is determined to be

$$\hat{u}_{mn}(x) = \sum_{j=1}^{n} \hat{c}_j \psi_j^{\varepsilon,\rho}(x), \quad x \in \Omega. \tag{14}$$

3.2. Two-Dimensional VIEs

In two dimensions, e.g., $\Omega = [a, b] \times [c, d]$, VIEs may relate to problems like the Darboux hyperbolic PDE. The double integral in (12) is approximated via tensor-product CGL quadrature, resulting in:

$$\sum_{j=1}^{n} \hat{c}_j \psi_j^{\varepsilon,\rho}(x_i, t_i) - \lambda \sum_{q=1}^{P} \sum_{k=1}^{m} w_k \frac{\Delta y(x_i)}{2} \sum_{b=1}^{P} \sum_{r=1}^{m} w_r \frac{\Delta s(t_i)}{2}$$

$$\times K\left(x_i, t_i, \theta_k^q(x_i), \theta_r^b(t_i), \sum_{j=1}^{n} \hat{c}_j \psi_j^{\varepsilon,\rho}(\theta_k^q(x_i), \theta_r^b(t_i))\right) = f(x_i, t_i), \tag{15}$$

for $i = 1, \dots, n$, where $\Delta s(t_i) = \frac{t_i - c}{P}$, $\theta_r^b(t_i) = \frac{\Delta s(t_i)}{2} v_r + (b - \frac{1}{2})\Delta s(t_i)$, and $\psi_j^{\varepsilon,\rho}(x, t) = \psi^{\varepsilon,\rho}(\sqrt{(x - x_j)^2 + (t - t_j)^2})$. Ultimately, by solving (15) for the unknowns $\{\hat{c}_j\}_{j=1}^{n}$, the values of $u(x, t)$ can be evaluated by

$$\hat{u}_{mn}(x, t) = \sum_{j=1}^{n} \hat{c}_j \psi_j^{\varepsilon,\rho}(x, t).$$

3.3. Higher-Dimensional VIEs

For $d \geq 3$, the d-dimensional integral in (12) uses d-fold CGL quadrature, producing:

$$\sum_{j=1}^{n} \hat{c}_j \psi_j^{\varepsilon,\rho}(\mathbf{x}_i) - \lambda \sum_{q=1}^{P} \sum_{k=1}^{m} \tilde{\mathbf{w}}_k K\left(\mathbf{x}_i, \boldsymbol{\theta}_k^q, \sum_{j=1}^{n} \hat{c}_j \psi_j^{\varepsilon,\rho}(\boldsymbol{\theta}_k^q)\right) = f(\mathbf{x}_i), \tag{16}$$

where $\{\tilde{\mathbf{w}}_k\}$ and $\{\boldsymbol{\theta}_k^q\}$ are d-dimensional weights and nodes. Solving this system, ultimately leads to the following numerical solution:

$$\hat{u}_{mn}(\mathbf{x}) = \sum_{j=1}^{n} \hat{c}_j \psi_j^{\varepsilon,\rho}(\mathbf{x}), \quad \mathbf{x} \in \Omega. \tag{17}$$

The HRK-based collocation method consistently balances accuracy and stability across dimensions, as explored further in subsequent sections.

Algorithm 1 Meshless HRK-Based Collocation Method for Solving VIEs
___
Require: Domain $\Omega = [a_1, b_1] \times \cdots \times [a_d, b_d] \subset \mathbb{R}^d$, number of collocation points n, HRK shape parameter ε, weight parameter ρ, base kernels $\Phi^\varepsilon(\mathbf{x})$ (infinitely smooth) and $\varphi(\mathbf{x})$ (piecewise smooth), functions $f(\mathbf{x})$ and $K(\mathbf{x}, \mathbf{y}, u)$, quadrature parameters m (points) and P (subdivisions)

Ensure: Approximate solution $\hat{u}_{mn}(\mathbf{x})$ for any $\mathbf{x} \in \Omega$

1: **Select Collocation Points:** Choose n distinct points $\mathcal{X} = \{\mathbf{x}_i\}_{i=1}^n \subset \Omega$ (e.g., uniformly spaced or scattered).

2: **Define Hybrid Radial Kernels (HRKs):** For each $\mathbf{x}_j$, define

$$\psi_j^{\varepsilon, \rho}(\mathbf{x}) = \Phi^\varepsilon(\mathbf{x} - \mathbf{x}_j) + \rho \varphi(\mathbf{x} - \mathbf{x}_j),$$

in which Φ^ε is an infinitely smooth kernel (e.g., Gaussian) and φ is a piecewise smooth kernel (e.g., cubic spline).

3: **Set Up the Collocation System:** Approximate the solution as

$$u_n(\mathbf{x}) = \sum_{j=1}^n c_j \psi_j^{\varepsilon, \rho}(\mathbf{x}),$$

and enforce the VIE at each $\mathbf{x}_i$:

$$\sum_{j=1}^n c_j \psi_j^{\varepsilon, \rho}(\mathbf{x}_i) - \lambda \int_{a_1}^{x_{i1}} \cdots \int_{a_d}^{x_{id}} K\left(\mathbf{x}_i, \mathbf{y}, \sum_{j=1}^n c_j \psi_j^{\varepsilon, \rho}(\mathbf{y})\right) d\mathbf{y} = f(\mathbf{x}_i), \quad i = 1, \ldots, n.$$

4: **Numerically Integrate the Integral Term:**

5: **if** $d = 1$ **then**

6:   Use CGL quadrature with m points and P subdivisions over $[a, x_i]$:

$$\int_a^{x_i} K\left(x_i, t, \sum_{j=1}^n c_j \psi_j^{\varepsilon, \rho}(t)\right) dt \approx \sum_{q=1}^P \sum_{k=1}^m w_k \frac{\Delta y(x_i)}{2} K\left(x_i, \theta_k^q(x_i), \sum_{j=1}^n c_j \psi_j^{\varepsilon, \rho}(\theta_k^q(x_i))\right),$$

in which $\Delta y(x_i) = \frac{x_i - a}{P}$, $\theta_k^q(x_i) = \frac{\Delta y(x_i)}{2} v_k + \left(q - \frac{1}{2}\right) \Delta y(x_i)$, and $\{v_k, w_k\}$ are Gauss-Legendre nodes and weights.

7: **else if** $d = 2$ **then**

8:   Use tensor-product CGL quadrature over $[a, x_i] \times [c, t_i]$.

9: **else** $(d \geq 3)$

10:   Extend to d-fold CGL quadrature.

11: **Form the Nonlinear System:** Substitute the quadrature into the collocation equations to obtain

$$\mathbf{F}(\hat{\mathbf{c}}) = \mathbf{0},$$

where $\hat{\mathbf{c}} = [\hat{c}_1, \ldots, \hat{c}_n]^T$.

12: **Solve the Nonlinear System:** Use an iterative solver (e.g., Newton's method) to find $\hat{\mathbf{c}}$,

13: **Construct the Approximate Solution:** Compute

$$\hat{u}_{mn}(\mathbf{x}) = \sum_{j=1}^n \hat{c}_j \psi_j^{\varepsilon, \rho}(\mathbf{x}).$$

14: **(Optional) Optimize Parameters:** Adjust ε and ρ (e.g., via particle swarm optimization)
___

4. Analytical Convergence Results

This part examines the convergence and accuracy of the HRK-based collocation approach for nonlinear VIEs. This discussion is primarily derived from [45].

The collocation operator $\mathcal{Q}_n : \mathcal{N}_{\psi^{\varepsilon,\rho}}(\Omega) \to C_n(\Omega)$ is given by:

$$\mathcal{Q}_n u(\mathbf{x}) = \sum_{k=1}^{n} c_k \psi^{\varepsilon,\rho}(\|\mathbf{x} - \mathbf{x}_k\|_2), \quad \mathbf{x} \in \Omega, \tag{18}$$

in which $C_n(\Omega) = \operatorname{span}\{\psi^{\varepsilon,\rho}(\|\mathbf{x} - \mathbf{x}_1\|_2), \ldots, \psi^{\varepsilon,\rho}(\|\mathbf{x} - \mathbf{x}_n\|_2)\}$.

The numerical scheme approximates the VIE via:

$$\mathcal{Q}_n \mathcal{F}_m \hat{u}_{mn} = \hat{u}_{mn}, \tag{19}$$

where $\mathcal{F}_m$ is a numerical integral operator. Also, for $u \in C^{2m}(\Omega)$ and $K \in C^{2m}(\Omega \times \Omega \times \mathbb{R})$, the error satisfies:

$$\|\mathcal{F}u - \mathcal{F}_m u\|_\infty \leq \frac{C_m}{P^{2m}} \sup_{\mathbf{x} \in \Omega} |u^{(2m)}(\mathbf{x})|, \tag{20}$$

with C_m tied to regularity parameters [46].

Using the Mean-Value Theorem, for some $\xi(\mathbf{y})$ between $u(\mathbf{y})$ and $\hat{u}_n(\mathbf{y})$:

$$K(\mathbf{x}, \mathbf{y}, u(\mathbf{y})) - K(\mathbf{x}, \mathbf{y}, \hat{u}_n(\mathbf{y})) = K_u(\mathbf{x}, \mathbf{y}, \xi(\mathbf{y}))(u - \hat{u}_n)(\mathbf{y}). \tag{21}$$

Define operators $\mathcal{W}_1, \mathcal{W}_2 : C(\Omega) \to C(\Omega)$ via quadrature:

$$\mathcal{W}_1 \psi^{\varepsilon,\rho}(\mathbf{x}) = \int_\Omega K_u(\mathbf{x}, \mathbf{y}, u(\mathbf{y})) \psi^{\varepsilon,\rho}(\mathbf{y}) \, d\mathbf{y}, \tag{22}$$

$$\mathcal{W}_2 \psi^{\varepsilon,\rho}(\mathbf{x}) = \int_\Omega K_u(\mathbf{x}, \mathbf{y}, \xi(\mathbf{y})) \psi^{\varepsilon,\rho}(\mathbf{y}) \, d\mathbf{y}, \tag{23}$$

approximated numerically as needed.

Throughout this paper, we resort to the standard hypothesis, such that $(\mathcal{I} - \mathcal{W}_1)^{-1}$ always exists and is bounded [44]. Based on the above assumptions, as $n \longrightarrow \infty$ we have [44]

$$\|\mathcal{W}_1 - \mathcal{W}_2\| \to 0, \quad \|(\mathcal{I} - \mathcal{Q}_n)\mathcal{W}_1\| \to 0. \tag{24}$$

The main convergence result is:

Theorem 3. *Assume the new scheme has been constricted on the quasi-uniform set $\mathcal{X} = \{\mathbf{x}_i\}_{i=1}^{n}$ on the domain Ω. Under the conditions of Corollary 1, for $u \in \mathcal{N}_{\Psi^{\varepsilon,\rho}}(\Omega) \cap C^{2m}(\Omega)$ solving the VIE with $K \in C^{2m}(\Omega \times \Omega \times \mathbb{R})$, the operator $(\mathcal{I} - \mathcal{Q}_n \mathcal{W}_2)^{-1}$ exists and is uniformly bounded for large n. The error satisfies:*

$$\|\hat{e}_{mn}\| \leq \alpha(\sigma \frac{C_m}{P^{2m}} \sup_{\mathbf{x} \in \Omega} |u^{(2m)}(\mathbf{x})| + \tilde{C}\sqrt{\tilde{C}_{\psi^{\varepsilon,\rho}}} h_{\mathcal{X},\Omega}^k \|u\|_{\mathcal{N}_{\psi^{\varepsilon,\rho}}(\Omega)}),$$

where $\alpha, \sigma, m, \tilde{C}, C_m$ are positive constants.

Proof. From (10), we have

$$\mathcal{Q}_n u = \mathcal{Q}_n \mathcal{F}u. \tag{25}$$

Now utilizing (19) leads to

$$\mathcal{Q}_n u - \hat{u}_{mn} = \mathcal{Q}_n(\mathcal{F}u - \mathcal{F}_m\hat{u}_{mn}) = \mathcal{Q}_n(\{\mathcal{F}u - \mathcal{F}_m u\} + \{\mathcal{F}_m u - \mathcal{F}_m\hat{u}_{mn}\}). \tag{26}$$

From (21), we have

$$\mathcal{F}_m u - \mathcal{F}_m\hat{u}_{mn} = \mathcal{W}_2\hat{e}_{mn} = \mathcal{W}_2(u - \hat{u}_{mn}). \tag{27}$$

Thus, we can write

$$(\mathcal{I} - \mathcal{Q}_n\mathcal{W}_2)\hat{u}_{mn} = \mathcal{Q}_n(u - \{\mathcal{F}u - \mathcal{F}_m u\} - \mathcal{W}_2 u), \tag{28}$$

or equivalently

$$(\mathcal{I} - \mathcal{Q}_n\mathcal{W}_2)\hat{e}_{mn} = \mathcal{Q}_n(\mathcal{F}u - \mathcal{F}_m u) + (\mathcal{Q}_n u - u). \tag{29}$$

To demonstrate the existence of $(\mathcal{I} - \mathcal{Q}_n\mathcal{W}_2)^{-1}$, we consider

$$\begin{aligned} \mathcal{I} - \mathcal{Q}_n\mathcal{W}_2 &= (\mathcal{I} - \mathcal{Q}_n\mathcal{W}_1) + \mathcal{Q}_n(\mathcal{W}_1 - \mathcal{W}_2) \\ &= (\mathcal{I} - \mathcal{W}_1) + (\mathcal{I} - \mathcal{Q}_n)\mathcal{W}_1 + \mathcal{Q}_n(\mathcal{W}_1 - \mathcal{W}_2) \\ &= (\mathcal{I} - \mathcal{W}_1)\{\mathcal{I} + (\mathcal{I} - \mathcal{W}_1)^{-1}[(\mathcal{I} - \mathcal{Q}_n)\mathcal{W}_1 + \mathcal{Q}_n(\mathcal{W}_1 - \mathcal{W}_2)]\}. \end{aligned}$$

From the existence and uniform boundedness of $(\mathcal{I} - \mathcal{W}_1)^{-1}$, and by applying (24), it follows that the operator $(\mathcal{I} - \mathcal{Q}_n\mathcal{W}_2)^{-1}$ also exists and remains uniformly bounded for sufficiently large n, i.e.,

$$\|(\mathcal{I} - \mathcal{Q}_n\mathcal{W}_2)^{-1}\| \leq \alpha, \tag{30}$$

in which α is a positive constant. Also, from (29) and the uniform boundedness of the family $\{\mathcal{Q}_n\}$ [23], namely

$$\sup_{n\geq 1}\|\mathcal{Q}_n\|_\infty \leq \sigma,$$

we have

$$\begin{aligned} \|\hat{e}_{mn}\| &\leq \|(\mathcal{I} - \mathcal{Q}_n\mathcal{W}_2)^{-1}\|\|\mathcal{Q}_n(\mathcal{F}u - \mathcal{F}_m u) + (\mathcal{Q}_n u - u)\| \\ &\leq \alpha(\sigma\|\mathcal{F}u - \mathcal{F}_m u\| + \|\mathcal{Q}_n u - u\|). \end{aligned}$$

Since $u \in \mathcal{N}_{\Psi^{\varepsilon,\rho}}(\Omega) \cap C^{2m}(\Omega)$ from (20) and Corollary 1, we have

$$\|\hat{e}_{mn}\| \leq \alpha(\sigma\frac{C_m}{P^{2m}}\sup_{\mathbf{x}\in\Omega}|u^{(2m)}(\mathbf{x})| + \tilde{C}\sqrt{\tilde{C}_{\psi^{\varepsilon,\rho}}}h_{\mathcal{X},\Omega}^k\|u\|_{\mathcal{N}_{\psi^{\varepsilon,\rho}}(\Omega)}).$$

$\square$

5. Novel Parameter Selection Methodology

This section presents an optimized approach for selecting the shape parameter ε and weight parameter ρ in HRKs, critical for balancing accuracy and stability in the meshless solution of VIEs.

5.1. Objective Function

The objective function for parameter optimization is the root-mean-square (RMS) error of the HRK interpolation:

$$O_f(\varepsilon, \rho) = \sqrt{\frac{1}{M} \sum_{j=1}^{M} \left[u(\zeta_j) - \tilde{u}_n(\zeta_j; \varepsilon, \rho) \right]^2},$$

where $\{\zeta_j\}_{j=1}^{M}$ are evaluation points in Ω, u is the exact solution, and $\tilde{u}_n(\cdot; \varepsilon, \rho)$ is the HRK-based interpolation from Section 3. The optimization problem is:

$$\text{Minimize } O_f(\varepsilon, \rho)$$
$$\text{subject to } 0 \leq \varepsilon \leq 10,$$
$$0 \leq \rho \leq 1,$$

where ε and ρ are the kernel parameters. The bounds for ε and ρ were chosen based on theoretical and empirical considerations. Theoretically, very small ε causes ill-conditioning, while very large ε reduces accuracy. On the other hand, the parameter ρ should be chosen sufficiently large to enhance numerical stability, while remaining small enough to ensure rapid convergence. Empirically, as shown in Section 6, the optimal solutions consistently lie within the chosen ranges $\varepsilon \in [0, 10]$ and $\rho \in [0, 1]$ and enlarging the bounds did not improve accuracy.

Remark 2. *Since the aim of the present paper is the comparison of the results of HRKs method for different VIEs, problems with existing exact solutions are considered. It must be emphasized that for practical problems where the exact solution is not known, it is not possible to calculate the exact RMS norm. In such situations, leave-one-out cross-validation (LOOCV) [47] is a prominent technique that can be used in conjunction with the PSO algorithm to find the optimal values of parameters.*

5.2. Parameter Optimization via PSO

Given the multimodal nature of O_f due to the interplay between ε and ρ in HRKs, we employ Particle Swarm Optimization (PSO) [48], a metaheuristic algorithm well-suited for non-convex problems. PSO iteratively refines a swarm of candidate solutions based on individual and collective best-known positions.

For HRK parameter selection, we adapt PSO with three modifications to enhance exploration and convergence:

- **Chaotic Initialization:** Particles are initialized using a logistic map [48] to ensure diversity across the parameter space:

$$z_{j+1} = \mu z_j (1 - z_j), \quad j = 1, 2, \ldots,$$

with $\mu = 4$ for full chaos, mapped to $[\varepsilon_{\min}, \varepsilon_{\max}]$ and $[\rho_{\min}, \rho_{\max}]$.

- **Sine Map for Inertia Weight:** The inertia weight w is adjusted dynamically using a sine map [48] to balance exploration and exploitation:

$$w_t = \frac{\nu}{4} \sin(\pi x_{t-1}), \quad x_t \in (0, 1), \quad 0 < \nu \leq 4,$$

where t is the iteration number.

- **Sine-Cosine Acceleration Coefficients:** Learning coefficients c_1 and c_2 are varied using sine and cosine functions to shift focus adaptively from cognitive to social learning:

$$c_1 = 2 + 0.5 \sin\left(\left(1 - \frac{t}{T}\right)\frac{\pi}{2}\right), \quad c_2 = 2 + 0.5 \cos\left(\left(1 - \frac{t}{T}\right)\frac{\pi}{2}\right),$$

where T is the maximum number of iterations [48].

These modifications enable PSO to navigate the complex parameter landscape of HRKs effectively, avoiding local minima and accelerating convergence to optimal (ε, ρ). The procedure is outlined in Figure 1, tailored to HRK parameter optimization. Also, the full implementation of the proposed PSO algorithm is publicly available at: [insert link here].

6. Numerical verification across dimensional cases

This section is devoted to testing the effectiveness and reliability of the hybrid method using numerical examples. For this study, the following combinations of radial kernels have been employed:

$$\psi_j^{\varepsilon,\rho}(r) = e^{-(\varepsilon r)^2} + \rho r^3 \quad (GA + CU),$$
$$\psi_j^{\varepsilon,\rho}(r) = \sqrt{\varepsilon^2 r^2 + 1} + \rho r^3 \quad (MQ + CU),$$
$$\psi_j^{\varepsilon,\rho}(r) = e^{-(\varepsilon r)^2} + \rho r^2 \log(r) \quad (GA + TPS),$$
$$\psi_j^{\varepsilon,\rho}(r) = \sqrt{\varepsilon^2 r^2 + 1} + \rho r^2 \log(r) \quad (MQ + TPS).$$

In each experiment, the population size was chosen as $n_P = 25$ and the iteration limit was fixed at $T = 60$. All calculations and plots have been done by "Maple 18" software and run on a Laptop with 1.70GHz of Core i5-4210U CPU and 6 GB of RAM.

Example 1. *Consider the nonlinear Lane–Emden equation that appears in the study of static stellar models within Newtonian gravity:*

$$y'' + \frac{2}{t}y' + y^5 = 0, \quad 0 < t \le 1,$$

subject to

$$y(0) = 1, \quad y'(0) = 0,$$

in which the exact solution is $y(x) = \left(1 + \frac{x^2}{3}\right)^{-1/2}$. This problem can be expressed as the following VIE [49]:

$$y(x) = 1 + \int_0^x \left(\frac{t^2}{x} - t\right) y^5(t)\, dt, \quad x \in (0, 1). \tag{31}$$

In this example, to approximate integrals, 5-point CGL integration scheme with $P = 5$ has been utilized. The performance results obtained through the PSO algorithm for various values of n are summarized in Table 2. Also, Figure 2 depicts the convergence behavior of the Gbest values associated with ρ and ε during the optimization process for $n = 4$. Furthermore, the convergence of the corresponding RMS errors is illustrated in Figure 2. For this figure, the parameters were set to $\varepsilon = 0.2$ and $\rho = 10^{-8}$. As shown in Figure 3, the GA+CU hybrid basis delivers the highest accuracy, outperforming MQ+CU, GA+TPS,
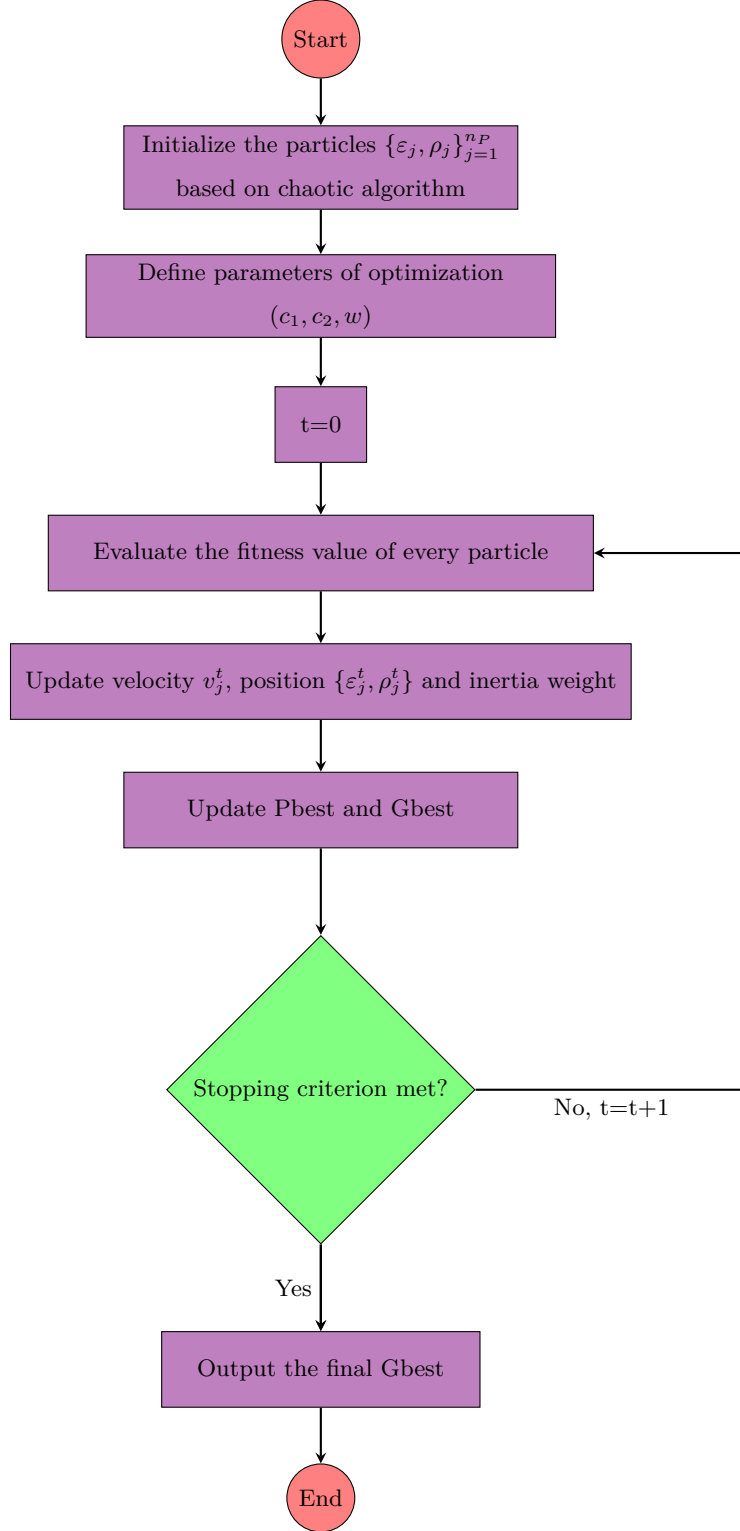
12

Figure 1: Flowchart illustrating the PSO algorithm implemented in this article.

and MQ+TPS in sequence. These findings confirm that hybrid kernels achieve greater accuracy than pure kernels. Also, Figure 4 explores the RMS error behavior as a function of $\varepsilon \in [0.02, 10]$ for varying ρ values, using both the pure GA kernel and GA+CU hybrid kernel with $n = 10$ on a log-log scale. The results indicate that at larger ρ values, the CU term dominates the GA term, which slows convergence. Conversely, smaller ρ values allow the GA term to prevail, resulting in improved accuracy. Notably, the lowest errors generally occur when the weight parameter ρ is small. In addition, Figure 4 highlights that the pure GA kernel ($\rho = 0$) loses accuracy when the shape parameter $\varepsilon \lesssim 1.6$. The GA+CU hybrid kernel, however, provides stable approximations across all shape parameter values. In this algorithm, ρ must be sufficiently large to enhance numerical stability while remaining small enough to allow rapid convergence. Overall, numerical results show that the hybridization of piecewise smooth radial kernels with infinitely smooth radial kernels remarkably reduced ill-conditioning and increased accuracy. For comparison purposes, we additionally solved integral equation (31) by applying the HS-SVD method [28] with kernels of Legendre, Brownian bridge, and Brownian motion type. The results, provided in Table 3, reveal that the proposed method achieves higher convergence rates and requires less CPU time compared to the HS-SVD method, further underscoring its computational efficiency and accuracy.

Table 2: Findings from the parameter optimization test for example 1 employing hybrid kernels.

| n	Hybrid kernel	ε_{opt}	ρ_{opt}	RMS error
4	GA+CU	0.3209	5.8012×10^{-8}	4.4339×10^{-5}
	MQ+CU	0.2957	1.8755×10^{-7}	1.7594×10^{-5}
	GA+TPS	0.3921	2.0367×10^{-6}	4.9284×10^{-5}
	MQ+TPS	0.2061	7.3254×10^{-8}	5.8312×10^{-5}
8	GA+CU	0.7027	4.2302×10^{-7}	2.5242×10^{-8}
	MQ+CU	0.3924	2.7581×10^{-9}	9.8593×10^{-8}
	GA+TPS	0.7186	3.2482×10^{-9}	2.7448×10^{-8}
	MQ+TPS	0.5594	2.4736×10^{-9}	1.7975×10^{-7}
12	GA+CU	0.9021	7.0068×10^{-10}	8.9070×10^{-10}
	MQ+CU	0.4275	1.1728×10^{-9}	1.3281×10^{-9}
	GA+TPS	0.6954	2.5921×10^{-10}	4.0667×10^{-9}
	MQ+TPS	0.3451	3.2103×10^{-10}	7.3687×10^{-9}
16	GA+CU	0.8011	3.0753×10^{-10}	2.4463×10^{-11}
	MQ+CU	0.4512	1.1729×10^{-10}	9.8760×10^{-11}
	GA+TPS	0.6541	4.0025×10^{-10}	4.1848×10^{-10}
	MQ+TPS	0.4102	2.7895×10^{-10}	8.9178×10^{-10}
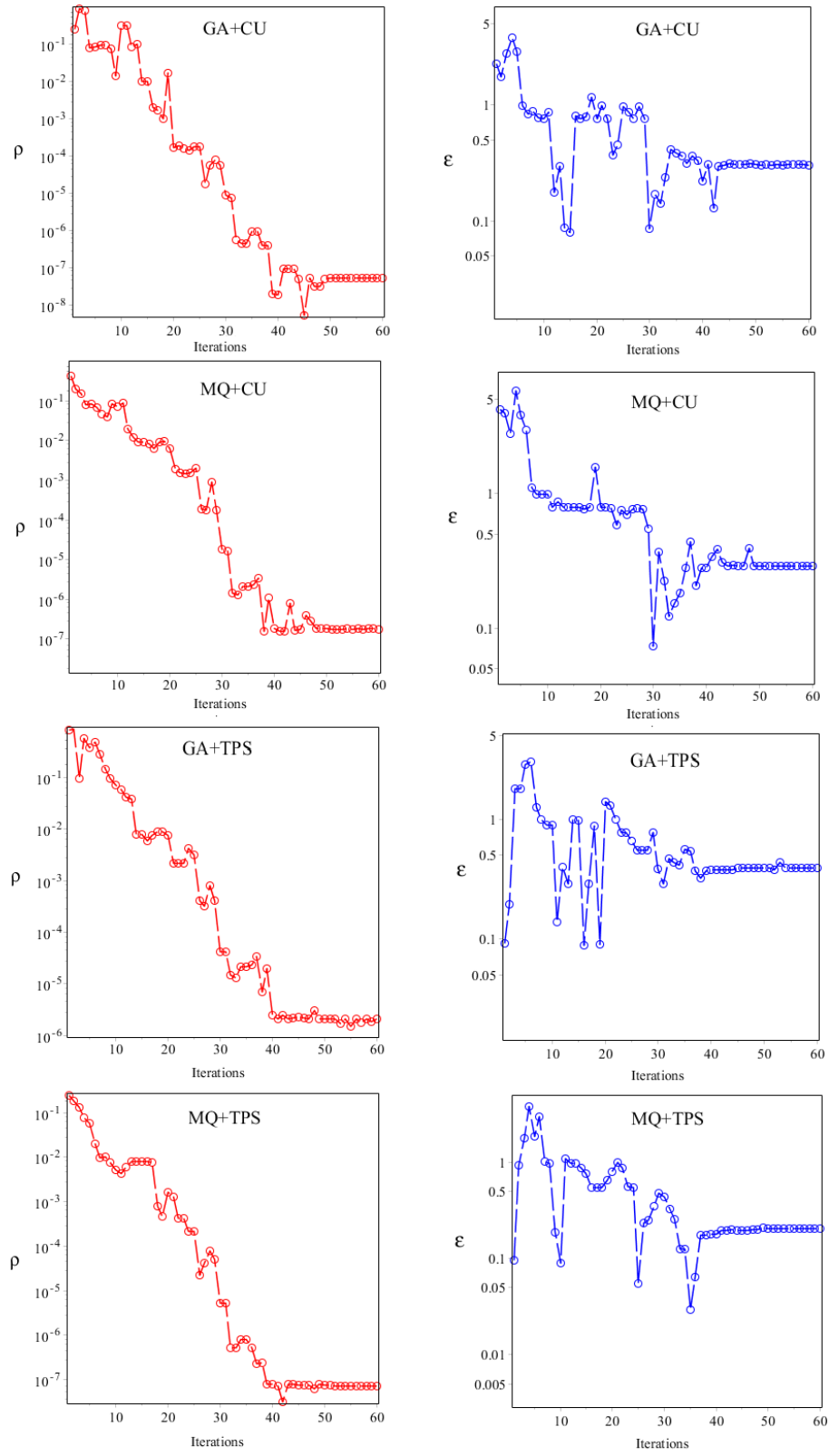
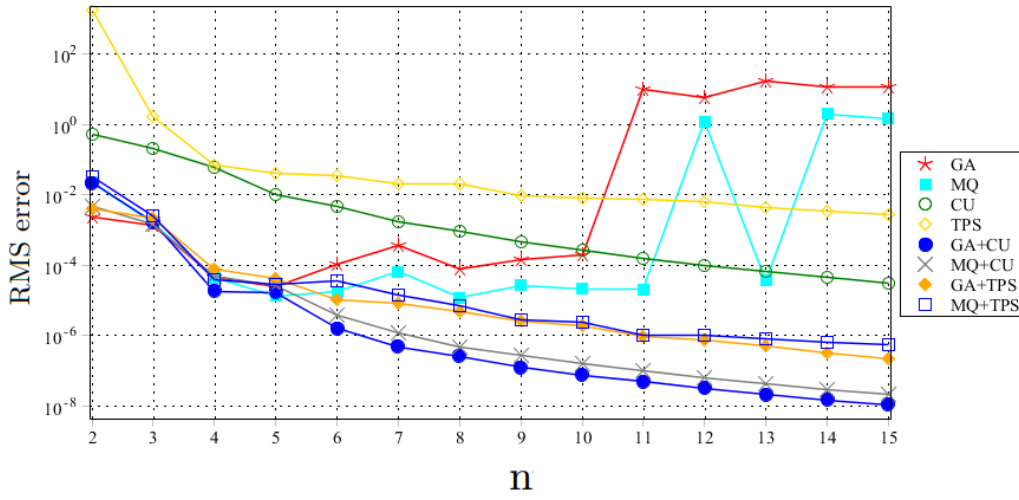Figure 2: Convergence of Gbest values for optimization of ρ and ε for $n = 4$ in Example 1.

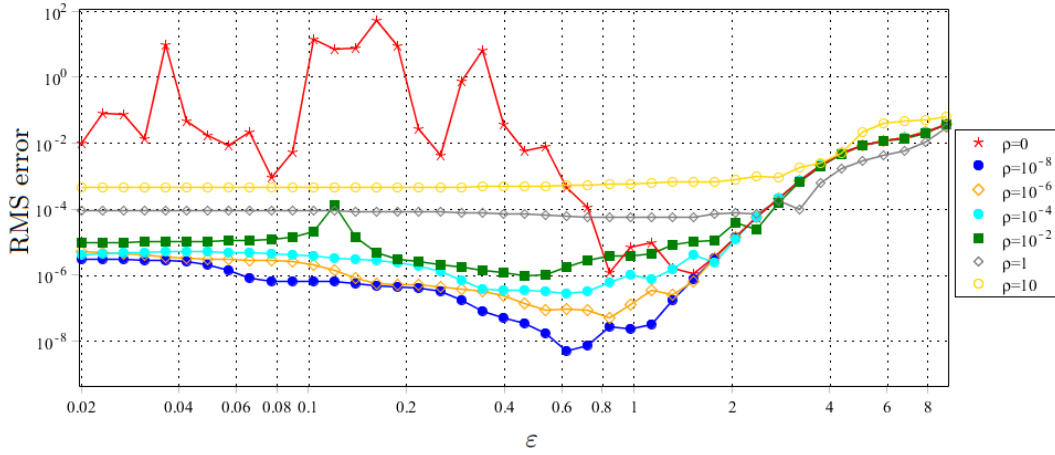Figure 3: RMS error convergence for different kernels.

Figure 4: RMS error convergence for various values of ρ.

Table 3: Errors produced by the HRK and HS-SVD approaches in example 1 when $n = 10$.

Methods	RMS-error	CPU Time
HS-SVD scheme based on the Legendre kernel	5.452×10^{-3}	25.71
HS-SVD scheme based on the Brownian bridge kernel	6.387×10^{-2}	28.41
HS-SVD scheme based on the Brownian motion kernel	3.712×10^{-3}	30.45
GA+CU - enhanced HRKs scheme ($\rho = 10^{-8}$, $\varepsilon = 1$)	6.656×10^{-7}	7.32
MQ+CU - enhanced HRKs scheme ($\rho = 10^{-8}$, $\varepsilon = 1$)	8.321×10^{-7}	7.14
GA+TPS - enhanced HRKs scheme ($\rho = 10^{-8}$, $\varepsilon = 1$)	2.078×10^{-6}	12.26
MQ+TPS - enhanced HRKs scheme ($\rho = 10^{-8}$, $\varepsilon = 1$)	3.314×10^{-6}	11.14

16

Example 2. *Consider the nonlinear VIE [2]*

$$u(x) = e^{-x} + \int_0^x e^{t-x}(u(t) + e^{-u(t)})dt, \tag{32}$$

with the exact solution $u(x) = \ln(x+e)$. Here, to approximate integrals, 10-point CGL integration scheme with $P = 5$ has been utilized. The performance results obtained through the PSO algorithm for various values of n are summarized in Table 4. Our observations indicate that the combination of GA and CU kernels demonstrates greater accuracy than other hybrid kernels. Furthermore, Figure 5 illustrates the convergence behavior of the Gbest values corresponding to ρ and ε throughout the optimization process for $n = 4$. Also, the absolute errors for $n = 10$ utilizing pure and hybrid kernels are displayed in Figure 6. In this figure, we employed the values $\rho = 10^{-10}$ and $\varepsilon = 0.2$. Furthermore, Figure 7 presents the RMS error values for values ε between 0.1 and 10, plotted on a log-log scale, for $n = 5, 10, 15$ using both GA and GA+TPS kernels. In this Figure, ρ is set to 10^{-9}. One can see that the results obtained with GA and GA+TPS kernels overlap when large enough values of ε are taken into account. Additionally, as the number of nodes n goes down, the overlapping region expands. Conversely, when n goes up, the overlapping region shrinks. Moreover, as ε tends to zero, the numerical results become more unstable when using a pure GA kernel. However, as compared to the pure GA kernel, the use of the GA and TPS kernel combination shows enhanced stability. For example, when $n = 15$, the results obtained using the pure GA kernel become unstable once ε drops below roughly 2.41. We can generally conclude that the error is significantly reduced when a small portion of a piecewise smooth radial kernel is combined with an infinitely smooth radial kernel. To evaluate the proposed method, integral equation (32) was also solved utilizing the HS-SVD approach with exponential kernel, and the numerical outcomes are summarized in Table 5. The exponential kernel in a closed form is representation by $\phi(x,t) = e^{(-\varepsilon|x-t|)}$. Our findings indicate that the hybrid kernel method converges more quickly than the HS-SVD strategy. In addition, the new approach attains greater accuracy than the HS-SVD mechanism while requiring fewer collocation nodes.

Table 4: Findings from the parameter optimization test for example 2 employing hybrid kernels.

n	Hybrid kernel	ε_{opt}	ρ_{opt}	RMS error
4	GA+CU	0.3472	3.2418×10^{-6}	7.3418×10^{-6}
	MQ+CU	0.2390	5.8012×10^{-6}	4.4339×10^{-5}
	GA+TPS	0.3476	3.5271×10^{-5}	5.9441×10^{-5}
	MQ+TPS	0.1491	7.3254×10^{-6}	7.8312×10^{-5}
8	GA+CU	0.4041	2.2145×10^{-10}	2.5411×10^{-8}
	MQ+CU	0.2195	4.2302×10^{-10}	2.9852×10^{-8}
	GA+TPS	0.4435	8.4123×10^{-9}	8.6564×10^{-8}
	MQ+TPS	0.2649	2.4736×10^{-8}	1.9878×10^{-7}
12	GA+CU	0.5886	1.2746×10^{-10}	5.1242×10^{-10}
	MQ+CU	0.3460	3.5491×10^{-10}	2.8314×10^{-9}
	GA+TPS	0.3641	9.2158×10^{-10}	6.5381×10^{-9}
	MQ+TPS	0.3190	2.8741×10^{-9}	1.6899×10^{-8}
16	GA+CU	0.5788	1.5231×10^{-10}	9.1284×10^{-11}
	MQ+CU	0.3476	2.3749×10^{-10}	5.8321×10^{-10}
	GA+TPS	0.6047	7.2475×10^{-10}	8.7135×10^{-10}
	MQ+TPS	0.5265	7.2475×10^{-9}	2.5901×10^{-9}

Table 5: Errors produced by the HRK and HS-SVD approaches in example 2 when $\varepsilon = 0.5$.

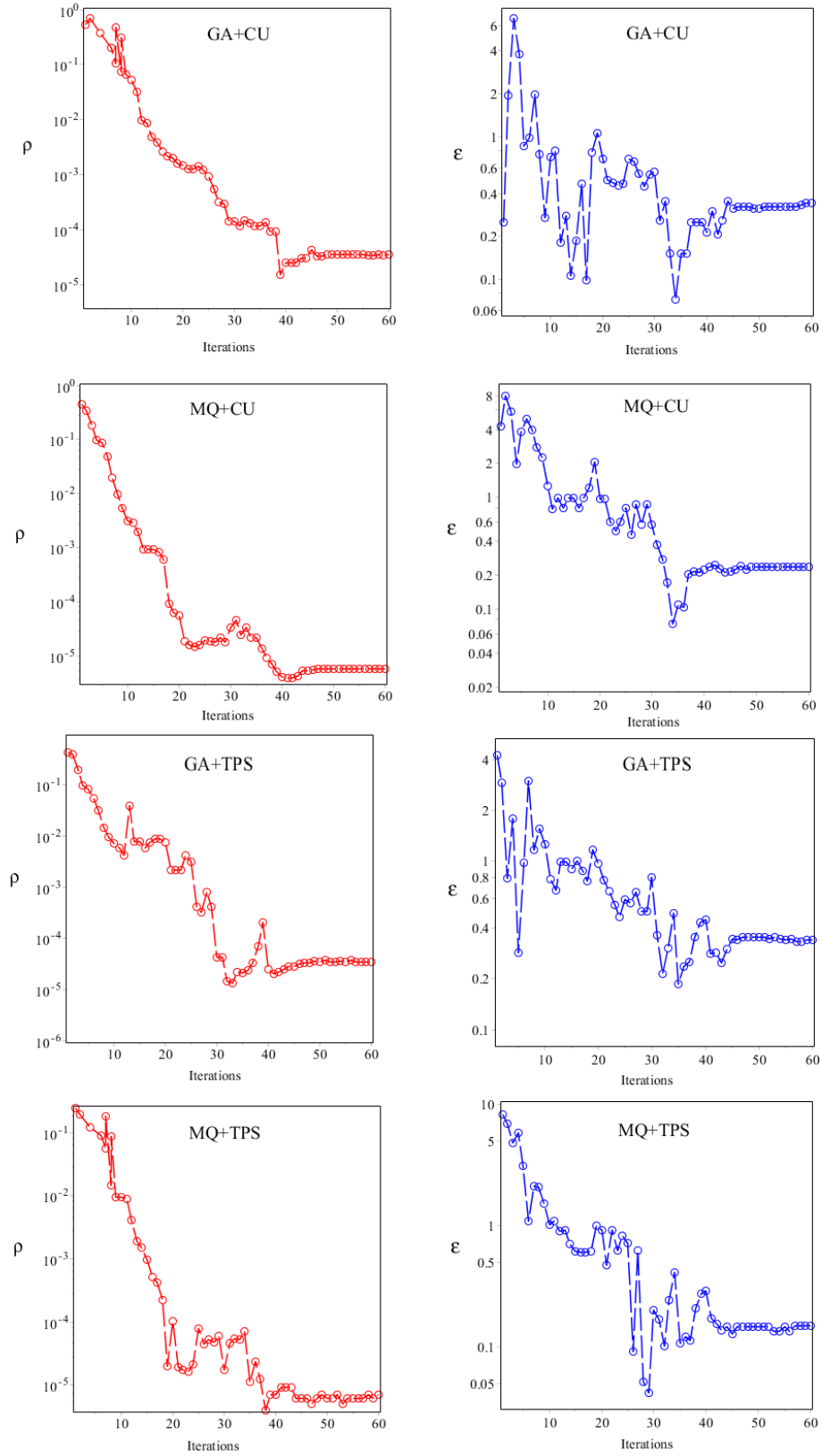| Methods	RMS-error	CPU Time
HS-SVD scheme based on the exponential kernel (n=10)	1.366×10^{-3}	24.68
HS-SVD scheme based on the exponential kernel (n=20)	7.411×10^{-4}	68.82
GA+CU - enhanced HRKs scheme ($\rho = 10^{-8}$, n=8)	6.0321×10^{-8}	5.76
MQ+CU - enhanced HRKs scheme ($\rho = 10^{-8}$, n=8)	1.135×10^{-7}	6.26
GA+TPS - enhanced HRKs scheme ($\rho = 10^{-8}$, n=8)	2.1024×10^{-7}	9.42
MQ+TPS - enhanced HRKs scheme ($\rho = 10^{-8}$, n=8)	5.6021×10^{-7}	8.17

Figure 5: Convergence of Gbest values for optimization of ρ and ε for $n = 4$ in Example 2.
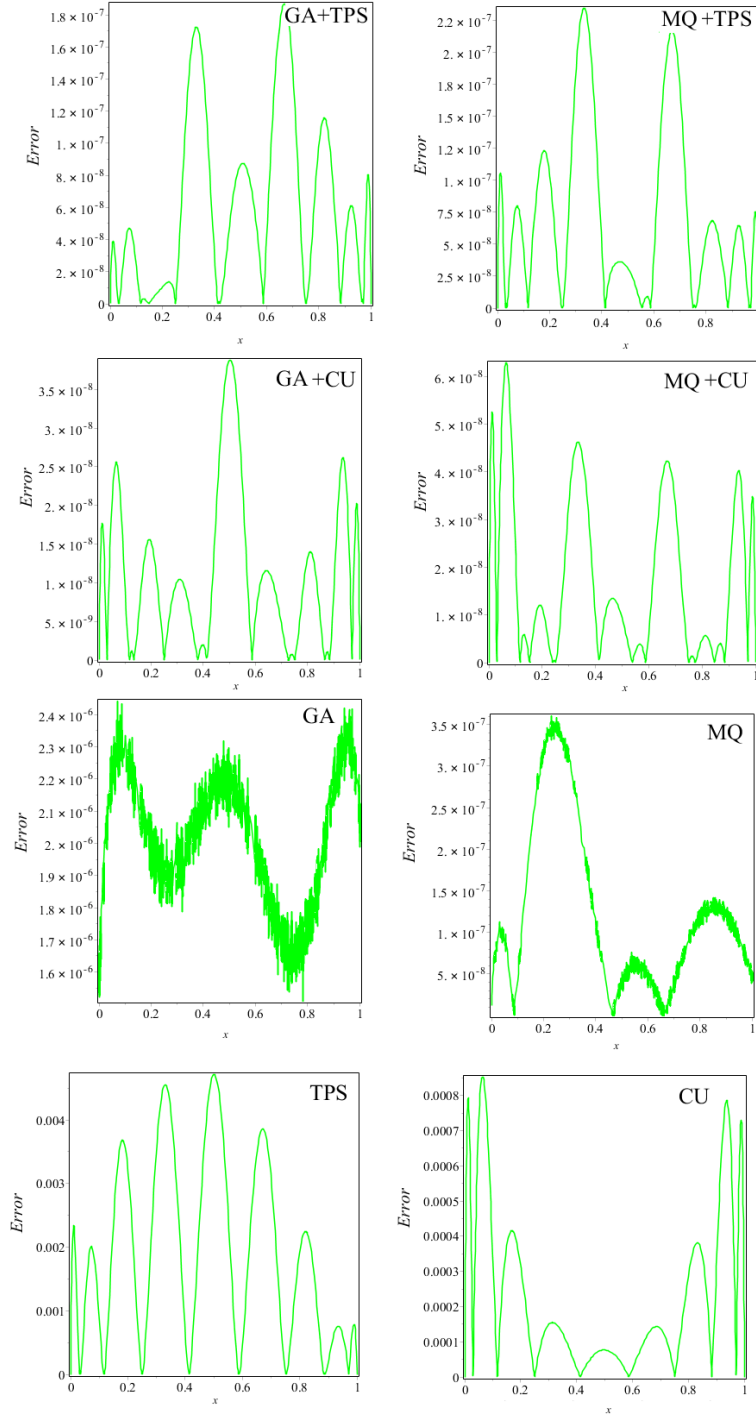
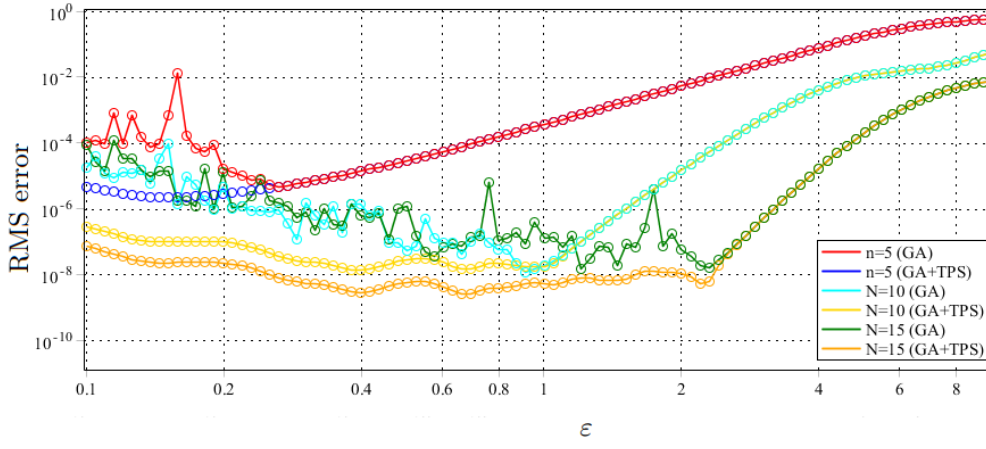19

Figure 6: Absolute error of example 2 with $n = 10$.

Figure 7: The RMS error, as a function of ε.

Example 3. *Consider the following second kind 2D-VIE [50]*

$$u(x,t) = f(x,t) + (x + t - z - y) \int_0^t \int_0^x u^2(y,z) dy dz, \quad (x,y) \in [0,1] \times [0,1], \tag{33}$$

in which

$$f(x,y) = x + t - \frac{1}{12} xt(x^3 + 4x^2 t + 4xt^2 + t^3).$$

The true solution is $u(x,t) = x + t$. In this example, to approximate integrals, 5-point CGL integration scheme with $P = 7$ has been utilized. The comparison of obtained errors by the offered hybrid approach and the rationalized Haar functions (RHFs) method [50] are given in Table 6. The numerical experiments have been carried out on the chosen grid points which are proposed as $(x,t) = \left(\frac{1}{2^l}, \frac{1}{2^l}\right), l = 1, 2, \cdots, 6$. This table illustrates that the new approach achieves greater accuracy than the RHFs method while utilizing fewer collocation nodes. Additionally, Figure 8 illustrates the convergence of RMS error for different kernels across various values of n. Since the MQ and GA kernels possess smoothness of high order, one might anticipate rapid convergence. Nevertheless, our experiments indicate that fixing the shape parameter ε causes the discretized system to suffer from increasing ill-conditioning as n grows. Consequently, for large n, accuracy does not improve significantly and the observed convergence rate deteriorates. By contrast, the TPS and CU kernels does not suffer this ill-conditioning due to their stability properties. However, the limited convergence rate is provided by the usage of these kernels. Additionally, hybrid kernels deliver greater accuracy compared to pure kernels. Figure 8 further shows that with increasing n, the GA+CU hybrid kernel achieves better performance than alternatives like MQ+CU, GA+TPS, and MQ+TPS. Overall, the experiments demonstrate that mixing piecewise smooth radial kernels with infinitely smooth ones yields notable gains in accuracy. Furthermore, Figure 9 provides a graphical illustration of the absolute error for different kernels when $n = 60$. In Figures 8 and 9, the parameters were set to $\varepsilon = 0.2$ and $\rho = 10^{-10}$.

Table 6: Comparison of the proposed hybrid method and RHFs method [50] for example 3.

$(x,t)=\left(\frac{1}{2^l},\frac{1}{2^l}\right)$	RHFs method [50]		Presented method ($n = 60$)	
	$\alpha = 3$ ($n = 256$)	$\alpha = 6$ ($n = 1024$)	GA+CU ($\varepsilon_{opt} = 0.42, \rho_{opt} = 4.7 \times 10^{-10}$)	MQ+CU ($\varepsilon_{opt} = 0.76, \rho_{opt} = 7.8 \times 10^{-9}$)
$l = 1$	6.2×10^{-2}	3.1×10^{-2}	2.4×10^{-13}	3.8×10^{-12}
$l = 2$	6.2×10^{-2}	3.1×10^{-2}	5.9×10^{-9}	1.5×10^{-8}
$l = 3$	6.2×10^{-2}	3.1×10^{-2}	8.2×10^{-8}	6.1×10^{-9}
$l = 4$	6.2×10^{-2}	3.1×10^{-2}	2.2×10^{-10}	4.2×10^{-8}
$l = 5$	6.9×10^{-8}	3.1×10^{-2}	1.1×10^{-8}	1.7×10^{-8}
$l = 6$	3.1×10^{-2}	2.2×10^{-9}	3.4×10^{-8}	3.9×10^{-8}
L_∞-error	1.72×10^{-3}	4.58×10^{-4}	3.4×10^{-7}	9.1×10^{-7}

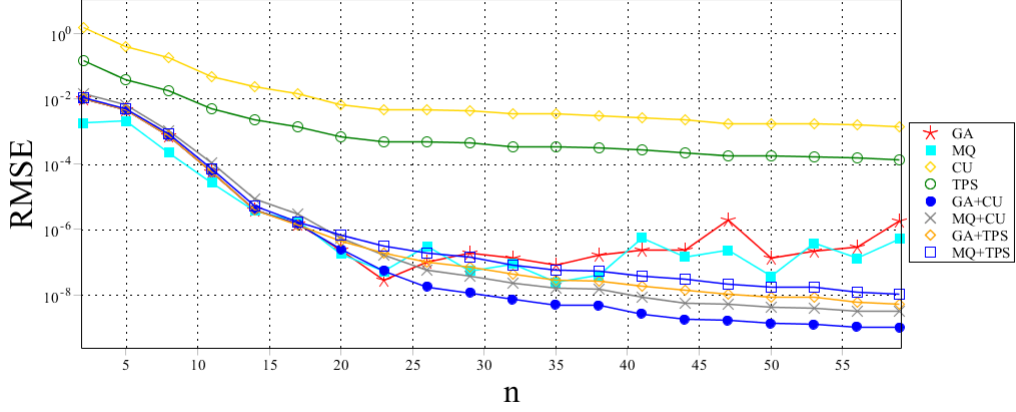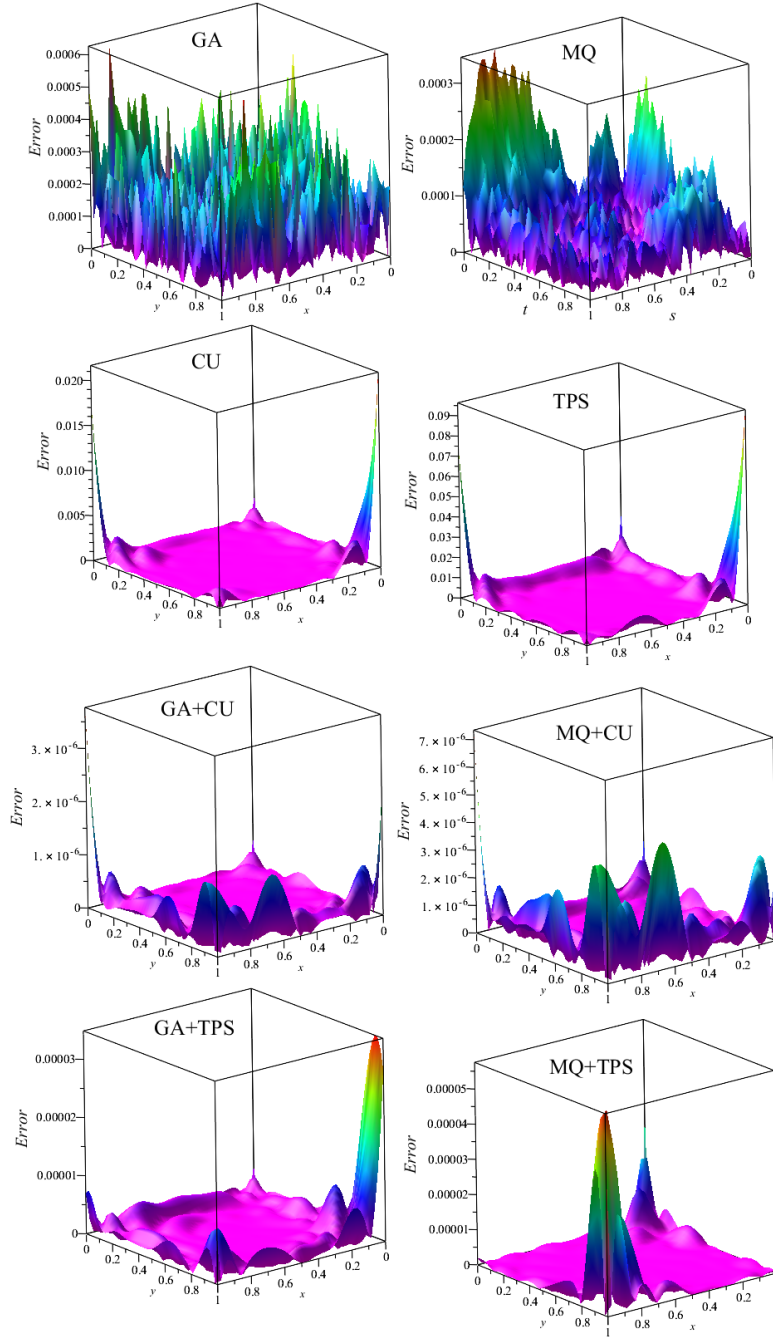Figure 8: RMS error convergence for different kernels.

Figure 9: Absolute error in example 3 for various kernels with $n = 60$.

7. Conclusions and future directions

This work introduces a stable mesh-free method based on hybrid radial kernels to approximate solutions of nonlinear VIEs of the second kind. The proposed technique applies HRKs to scattered nodes within a collocation scheme, with integrals approximated via the CGL integration rule. The combination of different kernel types improves both stability and adaptability, enabling efficient computation even for small shape parameters and higher degrees of freedom. By transforming the VIE into a system of nonlinear algebraic equations, the method is supported by a convergence analysis. The PSO algorithm is utilized to optimize the shape parameter and weight coefficient within the hybrid kernels. The numer-

23

ical results highlight the superior performance of the hybrid kernel approach over pure kernel methods, particularly as the number of nodes increases. Incorporating a small proportion of piecewise smooth radial kernels into infinitely smooth radial kernels markedly decreases errors, thereby improving accuracy. Additionally, the HRK-based method adapts seamlessly to various geometries, because of its independence from background meshes or cell structures, making it a versatile tool for solving VIEs in complex domains. While the offered approach mitigates the ill-conditioning challenges inherent in standard kernel approaches, it remains susceptible to potential ill-conditioning due to its global nature. Although hybrid kernels reduce sensitivity to the shape parameter, they do not completely eliminate it. Future research should aim to improve the stability of the method, potentially through the integration of local approximation techniques or the development of adaptive parameter selection strategies. Extending the approach to higher-dimensional problems and investigating its applicability to other classes of integral equations represent promising directions for further exploration.

Conflict of interest The authors declare that they have no competing interests.

References

[1] P. Assari, F. Asadi-Mehregan, M. Dehghan, On the numerical solution of Fredholm integral equations utilizing the local radial basis function method, Int. J. Comput. Math. 96 (2019) 1416–1443.

[2] C. T. Sheng, Z. Q. Wang, B. Y. Guo, A multistep Legendre–Gauss spectral collocation method for nonlinear Volterra integral equations, SIAM J. Numer. Anal. 52 (2014) 1953–1980.

[3] M. Heydari, E. Shivanian, B. Azarnavid, S. Abbasbandy, An iterative multistep kernel based method for nonlinear Volterra integral and integro-differential equations of fractional order, J. Comput. Appl. Math. 361 (2019) 97–112.

[4] A. M. Rismani, H. Monfared, Numerical solution of singular IVPs of Lane–Emden type using a modified Legendre-spectral method, Appl. Math. Model. 36 (2012) 4830–4836.

[5] C. T. Sheng, Z. Q. Wang, B. Y. Guo, An hp-spectral collocation method for nonlinear Volterra functional integro-differential equations with delays, Appl. Numer. Math. 105 (2016) 1–24.

[6] Y. Yang, Y. Chen, Jacobi spectral Galerkin and iterated methods for nonlinear Volterra integral equation, J. Comput. Nonlinear Dyn. 11 (4) (2016) 041027.

[7] P. Assari, M. Dehghan, A meshless local discrete Galerkin (MLDG) scheme for numerically solving two-dimensional nonlinear Volterra integral equations, Appl. Math. Comput. 350 (2019) 249–265.

[8] K. Maleknejad, R. Dehbozorgi, Adaptive numerical approach based upon Chebyshev operational vector for nonlinear Volterra integral equations and its convergence analysis, J. Comput. Appl. Math. 344 (2018) 356–366.

[9] S. Sohrabi, H. Ranjbar, M. Saei, Convergence analysis of the Jacobi-collocation method for nonlinear weakly singular Volterra integral equations, Appl. Math. Comput. 299 (2017) 141–152.

[10] H. Saeedi, M. M. Moghadam, Numerical solution of nonlinear Volterra integro-differential equations of arbitrary order by CAS wavelets, Commun. Nonlinear Sci. Numer. Simul. 16 (3) (2011) 1216–1226.

[11] I. Aziz, S.-u. Islam, New algorithms for the numerical solution of nonlinear Fredholm and Volterra integral equations using Haar wavelets, J. Comput. Appl. Math. 239 (2013) 333–345.

[12] S.-u. Islam, I. Aziz, A. S. Al-Fhaid, An improved method based on Haar wavelets for numerical solution of nonlinear integral and integro-differential equations of first and higher orders, J. Comput. Appl. Math. 260 (2014) 449–469.

[13] I. Aziz, S.-u. Islam, F. Khan, A new method based on Haar wavelet for the numerical solution of two-dimensional nonlinear integral equations, J. Comput. Appl. Math. 272 (2014) 70–80.

[14] E. Babolian, S. Javadi, E. Moradi, Error analysis of reproducing kernel Hilbert space method for solving functional integral equations, J. Comput. Appl. Math. 300 (2016) 300–311.

[15] V. Sizikov, D. Sidorov, Generalized quadrature for solving singular integral equations of Abel type in application to infrared tomography, Appl. Numer. Math. 106 (2016) 69–78.

[16] M. I. Berenguer, D. Gamez, A computational method for solving a class of two dimensional Volterra integral equations, J. Comput. Appl. Math. 318 (2017) 403–410.

[17] R. L. Hardy, Multiquadric equations of topography and other irregular surfaces, Geophys. Res. 76 (8) (1971) 1905–1915.

[18] J. Meinguet, Multivariate interpolation at arbitrary points made simple, Appl. Math. Phys. (ZAMP) 30 (1979) 292–304.

[19] B. Shaback, Meshfree methods for complicated domains and moving boundaries in solid mechanics, Eng. Anal. Bound. Elem. 32 (2008) 533–553.

[20] D. Stevens, H. Power, RBF-FD for Shallow Water Equations, J. Comput. Phys. 342 (2017) 86–105.

[21] B. Sarler, G. Kuhn, RBF Solution of Stefan Problems, Eng. Anal. Bound. Elem. 87 (2018) 1-12.

[22] S. N. Atluri, S. Shen, The meshless local Petrov–Galerkin (MLPG) method, CMES-Comput. Model. Eng. Sci. 3 (2002) 11–52.

[23] P. Assari, M. Dehghan, The approximate solution of nonlinear Volterra integral equations of the second kind using radial basis functions, Appl. Numer. Math. 131 (2018) 140-157.

[24] P. Assari, M. Dehghan, A meshless local Galerkin method for solving Volterra integral equations deduced from nonlinear fractional differential equations using the moving least squares technique, Appl. Numer. Math. 143 (2019) 276-299.

[25] M. Heidari, M. Mohammadi, S. De Marchi, Curvature based characterization of radial basis functions: application to interpolation, Math. Model. Anal. 28 (3) (2023) 415–433.

[26] F. N. Mojarrad, M. H. Veiga, J. S. Hesthaven, A new variable shape parameter strategy for RBF approximation using neural networks, Comput. Math. Appl. 143 (2023) 151–168.

[27] R. Cavoretto, S. De Rossi, S. Lancellotti, Bayesian approach for radial kernel parameter tuning, J. Comput. Appl. Math. 441 (2024) 115716.

[28] G. Fasshauer, M. McCourt, Kernel-Based Approximation Methods using MATLAB, World Scientific, Interdisciplinary Mathematical Sciences, 2015.

[29] R. Cavoretto, G. E. Fasshauer, M. McCourt, An introduction to the Hilbert-Schmidt SVD using iterated Brownian bridge kernels, Numer. Algor. 68 (2) (2015) 393–422.

[30] G. E. Fasshauer, M. J. McCourt, Stable evaluation of Gaussian radial basis function interpolants, SIAM J. Sci. Comput. 34 (2) (2012) A737–A762.

[31] P. K. Mishra, S. K. Nath, G. Kosec, G. E. Fasshauer, Hybrid Gaussian-cubic radial basis functions for scattered data interpolation, Comput. Geosci. 22 (5) (2018) 1203–1218.

[32] Y. Yang, X. Qingyu, L. Qiude, W. Chao, G. Min, W. Kai, A hybrid kernel function approach for acoustic reconstruction of temperature distribution, Measurement 166 (2020) 108238.

[33] O. Ömer, A local hybrid kernel meshless method for numerical solutions of two-dimensional fractional cable equation in neuronal dynamics, Numer. Methods Partial Differ. Equ. 36 (6) (2020) 1699–1717.

[34] H. Manzoor, Hybrid radial basis function methods of lines for the numerical solution of viscous Burgers' equation, Comput. Appl. Math. 40 (2021) 1–49.

[35] T. Akbari, M. Esmaeilbeigi, D. Moazami, A stable meshless numerical scheme using hybrid kernels to solve linear Fredholm integral equations of the second kind and its applications, Math. Comput. Simul. 220 (2024) 1–28.

[36] H. Wendland, Scattered data approximation, Cambridge University Press, 2005.

[37] M. Hussain, A. Ghafoor, A. Hussain, S. Haq, I. Ali, S. U. Arifeen, A hybrid kernel-based meshless method for numerical approximation of multidimensional Fisher's equation, Math. Comput. Simul. 223 (2024) 130–157.

[38] G. E. Fasshauer, Meshfree approximation methods with MATLAB, World Scientific Publishing Co., Inc., River Edge, NJ, USA, 2007.

[39] R. Cavoretto, A. De Rossi, M. S. Mukhametzhanov, Ya. D. Sergeyev, On the search of the shape parameter in radial basis functions using univariate global optimization methods, J. Glob. Optim. 79 (2019) 305–327.

[40] M. Hussain, S. Haq, A computational study of solitary waves solution of Kawahara-type equations by meshless spectral interpolation method, Int. J. Mod. Phys. C. 30 (12) (2019) 1950102.

[41] M. Hussain, S. Haq, Numerical simulation of solitary waves of Rosenau–KdV equation by Crank–Nicolson meshless spectral interpolation method, Eur. Phys. J. Plus. 98 (2020).

[42] S. A. Sarra, E. J. Kansa, Multiquadric radial basis function approximation methods for the numerical solution of partial differential equations, Adv. Comput. Mech. 2 (2009) 1940-5820.

[43] P. K. Mishra, G. E. Fasshauer, M. K. Sen, L. Ling, A stabilized radial basis-finite difference (RBF-FD) method with hybrid kernels, Comput. Math. Appl. 77(9) (2019) 2354–2368.

[44] S. Zhang, Y. Lin, M. Rao, Numerical solutions for second-kind Volterra integral equations by Galerkin methods, Appl. Math. 45 (2000) 19–39.

[45] M. D. Buhmann, Radial Basis Functions: Theory and Implementations, Cambridge University Press, Cambridge, 2003.

[46] W. Fang, Y. Wang, Y. Xu, An implementation of fast wavelet Galerkin methods for integral equations of the second kind, J. Sci. Comput. 20 (2004) 277–302.

[47] S. Rippa, An algorithm for selecting a good value for the parameter c in radial basis function interpolation, Adv. Comput. Math. 11(2-3) (1990) 193–210.

[48] D. Moazami, M. Esmaeilbeigi, Enhanced stability and accuracy in solving nonlinear Fredholm integral equations using hybrid radial kernels and particle swarm optimization, Comput. Appl. Math. 44 (78) (2025).

[49] B. Azarnavid, F. Parvaneh, S. Abbasbandy, Picard-reproducing kernel Hilbert space method for solving generalized singular nonlinear Lane–Emden type equations, Math. Model. Anal. 20 (6) (2015) 754–767.

[50] E. Babolian, S. Bazm, P. Lima, Numerical solution of nonlinear two-dimensional integral equations using rationalized Haar functions, Commun. Nonlinear Sci. Numer. Simul. 16 (2011) 1164–1175.